Automatic determination of vertical cup-to-disc ratio in retinal fundus images for glaucoma screening

Guo, Jiapan; Azzopardi, George; Shi, Chenyu; Jansonius, Nomdo M.; Petkov, Nicolai

Published in:
IEEE Access

DOI:
10.1109/ACCESS.2018.2890544

IEEE Access
Multidisciplinary | Rapid Review | Open Access Journal

Received December 7, 2018, accepted December 27, 2018, date of publication January 1, 2019, date of current version January 23, 2019.

Digital Object Identifier 10.1109/ACCESS.2018.2890544

Automatic Determination of Vertical Cup-to-Disc Ratio in Retinal Fundus Images for Glaucoma Screening

JIAPAN GUO[1], GEORGE AZZOPARDI[1], CHENYU SHI[1], NOMDO M. JANSONIUS[2], AND NICOLAI PETKOV[1]

[1]Bernoulli Institute for Mathematics, Computer Science and Artificial Intelligence, University of Groningen, 9747 AG Groningen, The Netherlands
[2]Department of Ophthalmology, University Medical Center Groningen, University of Groningen, 9713 GW Groningen, The Netherlands

Corresponding author : Chenyu Shi (scycau@gmail.com)

ABSTRACT Glaucoma is a chronic progressive optic neuropathy that causes visual impairment or blindness if left untreated. It is crucial to diagnose it at an early stage in order to enable treatment. Fundus photography is a viable option for population-based screening. A fundus photograph enables the observation of the excavation of the optic disk—the hallmark of glaucoma. The excavation is quantified as a vertical cup-to-disk ratio (VCDR). The manual assessment of retinal fundus images is, however, time-consuming and costly. Thus, an automated system is necessary to assist human observers. We propose a computer-aided diagnosis system, which consists of the localization of the optic disk, the determination of the height of the optic disk and the cup, and the computation of the VCDR. We evaluated the performance of our approach on eight publicly available datasets, which have, in total, 1712 retinal fundus images. We compared the obtained VCDR values with those provided by an experienced ophthalmologist and achieved a weighted VCDR mean difference of 0.11. The system provides a reliable estimation of the height of the optic disk and the cup in terms of the relative height error (RHE = 0.08 and 0.09, respectively). The Bland–Altman analysis showed that the system achieves a good agreement with the manual annotations, especially for large VCDRs which indicate pathology.

INDEX TERMS Glaucoma, retinal fundus images, vertical cup-to-disk ratio, trainable COSFIRE filters, GMLVQ.

I. INTRODUCTION

Glaucoma is a chronic, progressive neuropathy that affects irreversibly the optic nerve, the neural fiber bundle that relays visual information from the eye to the brain. The worldwide number of people (aged 40-80 years) affected by glaucoma was estimated to be 64 million in the year 2013. This number is expected to increase to 76 million by 2020 and to 120 million by 2040 [1], [2]. Glaucoma affects 1 - 2% of the population and is now the second leading cause of blindness [1].

As glaucoma is initially asymptomatic and the damage is irreversible, it is important to diagnose it as early as possible in order to halt or slow down progression by adequate treatment - thus avoiding visual impairment or blindness. The diagnosis and treatment of glaucoma requires specialized physicians and sophisticated procedures, such as tonometry (assessment of intraocular pressure), ophthalmoscopy (assessment of the optic nerve), and perimetry (assessment of visual function). The initial detection of glaucoma, however, does not necessarily require all of these measurements; a single assessment of the nerve could already be very valuable in a population-based screening setting. In addition to ophthalmoscopy by a skilled professional, fundus photography and optical coherence tomography (OCT) can be used for this assessment. With these techniques, the changes of the optic nerve head (ONH) and the retinal nerve fiber layer (RNFL) can be observed [3]. OCT enables a quantitative evaluation of individual retinal layers, including layers relevant to glaucoma. It is also useful to uncover certain aspects of macular degeneration and diabetic retinopathy. Compared to fundus photography, however, OCT is costly.

Fundus photography forms the cornerstone for the classification and grading of macular degeneration and diabetic retinopathy in (genetic) epidemiological research, and can also be used for the assessment of glaucoma [4]. A major

advantage of fundus photography is the availability in virtually all large eye studies, in which a detailed description of the characteristics and genotype of the participants is present as well [5]–[10]. Therefore, in this study we focus on fundus photography.

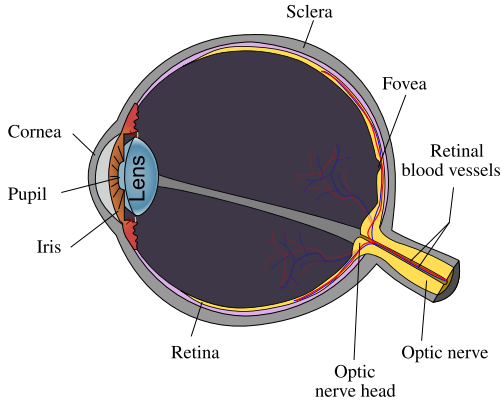

FIGURE 1. A schematic diagram of the human eye. This figure is taken from: http://tinyurl.com/mtkglzh.

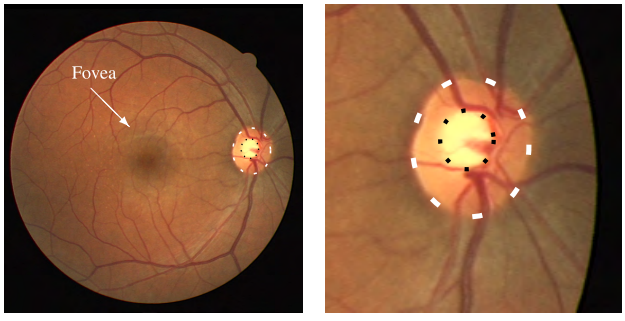

FIGURE 2. Example of a retinal fundus image and the optic nerve head. (a) A retinal fundus image (of size 564 × 584 pixels) captured at a field of view of 45° from a right eye. This image is taken from the DRIVE data set [11]. The white and black boundaries indicate the optic disk and the cup, respectively. The ring-shaped region between the black and the white boundaries is called neuroretinal rim. The vertical cup-to-disk ratio (VCDR) is 0.45. (b) A close-up view of the optic disk region.

Fig. 1 shows a schematic diagram that illustrates the anatomy of the human eye. The visual pathways start with the photoreceptors in the retina, which transduce light into neural signals. The photoreceptors relay information to bipolar cells that are connected to the retinal ganglion cells. The axons of the retinal ganglion cells leave the eye through the ONH. The ONH is also the entry point of the major blood vessels into the eye. Fig. 2a shows a retinal image taken with a fundus camera. The optic disk is the region surrounded by the dashed white boundary and is the two-dimensional view of the ONH. The optic disk appears as a bright reddish area which usually has a vertically elliptic shape [12]. Usually, three areas can be distinguished within the optic disk: a neuroretinal rim, a cup, and blood vessels. The cup is the pale, oval region in the middle

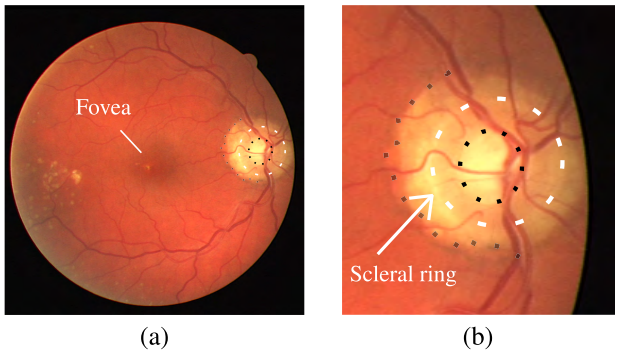

FIGURE 3. Example of a retina with pathology. (a) A retinal fundus image with pathologies that may make the optic disk look much bigger than it actually is. This image is taken from the DRIVE data set [11]. The real boundary of the optic disk is marked by the white-dashed contour. The light region between this boundary and the outer black dotted contour is due to the parapapillary atrophy. The VCDR value is 0.56. (b) A close-up view of the optic disk region.

of the optic disk, marked with the black dashed boundary. It is paler than the surrounding rim because - in contrast to the rim - it is void of optic nerve fibers. It is usually slightly decentered towards the fovea. The size of the cup relative to the size of the optic disk gives an indication of the state of the optic nerve. The vertical cup-to-disk ratio (VCDR), defined as the ratio between the height of the cup and that of the optic disk, is a commonly used measure to assess the state of the optic nerve and the risk of glaucoma [13]. Outside the optic disk sometimes there is a pale ring named scleral ring, which is indicated by the white arrow in Fig. 3b. Outside the scleral ring there is a yellow-gray region called parapapillary atrophy (PPA), as shown in Fig. 3(a-b). PPA is a glaucoma-related pathology that is due to the thinning of the layers of the retina and the retinal pigment epithelium around the optic disk. PPA and the scleral ring frustrate the correct determination of the optic disk border, making an accurate estimate of the VCDR difficult. For instance, the VCDR value of the retinal fundus image in Fig. 3(a-b) is 0.56. It can be underestimated if the observer erroneously determines the boundary of the optic disk as that of the PPA.

The manual analysis of retinal fundus images in glaucoma population screening would be a highly tedious procedure for medical experts, because of the large number of images of which only about five percent contain signs of glaucoma.[1] A computer-aided diagnosis system for glaucoma screening that measures the VCDR can be used to speed up the analysis of retinal images. Our decision to compute the VCDR of retinal images as opposed to methods [15]–[19] that address this challenge as a classification problem and provide only the likelihood that a given image is glaucomatous, is motivated by two main reasons. First, the VCDR is part of the current definition of glaucoma for epidemiological studies [20] and

[1]It is recommended for people above 40 years old to have regular eye examination. Among Caucasian people above this age the occurrence of glaucoma is approximately 2%, and it increases rapidly with age [14]. The occurrence is even higher in case of African descent.

still the preferred measure of glaucomatous optic neuropathy in these studies [21]. Second, the VCDR (and optic disk area) plays an important role in the unraveling of the genetics of glaucoma [22], and especially in genome-wide association studies, where a very large number (1,000-100,000) of fundus images have to be assessed. With the proposed work we contribute to the development of a feasible computer assisted screening program that would allow ophthalmologists to analyze the images based on the automatic computation of the VCDR.

In this work, we propose a computer-aided diagnosis system that uses trainable computer vision algorithms to estimate the VCDR in retinal fundus images. First, our system localizes the optic disk and approximates its boundary with an ellipse. We develop two novel shape-selective filters, namely the vasculature- and disk-selective COSFIRE filters and combine their results to provide a precise localization of the optic disk. We adapt such filters to the cases where parts of the patterns are missing or occluded, such as the vascular branches. Then, we fit an ellipse to the boundary of the optic disk and employ a Generalized Matrix Learning Vector Quantization classifier [23] to segment the optic disk into the optic neuroretinal rim and the cup. Finally, we compute the VCDR and provide a reliability indicator. Such a reliability indicator can be thought of as a confidence score of the resulting VCDR values as well as an indication of retinal abnormalities. We evaluate the proposed approach on eight public data sets and compare the obtained results with the manual annotation provided by a glaucoma expert from the University Medical Center Groningen. We also make the manual annotations from the glaucoma expert publicly available. The main contributions of this work are as follows:

(1) We propose a complete framework for the determination of the VCDR in retinal fundus images for glaucoma screening, which employs the visual features that are understandable and interpretable for the ophthalmologists.

(2) The proposed shape-selective COSFIRE filters for optic disk localization are configured based on the retinal fundus images in one data set, which show generalization ability also on images in other data sets with different imaging settings.

(3) The proposed approach is evaluated on eight public data sets which are easily accessible and the manual annotations will be available online for benchmarking purposes.

The rest of the paper is organized in the following way. In Section II, we review studies which attempted to solve the same problem or parts of it. In Section III we present our proposed method that determines the boundary of the optic disk and the cup and evaluates the VCDR. In Section IV we describe the data sets and the corresponding manual annotation followed by the experiments and the experimental results. Finally, we discuss some aspects of the proposed method in Section V and draw conclusions in Section VI.

II. RELATED WORK

The automatic detection of glaucoma has attracted the interest of many researchers [24]. Most of the studies, however, address only parts of the problem. For instance, some studies focus on the localization of the optic disk [25]–[33], and some also attempt to delineate the boundary of the optic disk [34]–[36]. Others focus on the segmentation of the cup [37]–[41] or some other features for the detection of glaucoma [15], [18], [42], [43].

The algorithms proposed for the localization and boundary detection of the optic disk can be categorized into two types, namely intensity-based and vasculature-based. The former methods detect the optic disk by its visual appearance which is characterized by a circular or an oval shape with bright luminosity. On the other hand, vasculature-based approaches analyze the position of the large retinal blood vessels that diverge from the interior of the optic disk.

Various approaches have been proposed to localize the optic disk as the brightest region in a retinal fundus image [26]–[28]. Sinthanayothin *et al.* [25] proposed a variance-based optic disk detection, in which the location of the optic disk is identified by the area of the highest variation in intensity. Walter and Klein [26] estimated the center of the optic disk as the center of the connected region with the highest brightness and then applied the watershed transform to the image gradient to obtain the disk boundary. Other intensity-based methods that extract shape information of the optic disk employ algorithms, such as circular Hough transform [35] and template matching [34]. These methods require images with even illumination and are not sufficiently robust for images with pathologies. In [29], it was demonstrated that the brightness, shape, and contrast are not robust features for optic disk detection in images with pathologies.

In order to avoid relying on the luminosity, other methods [29]–[31], [44] sought to analyze the vascular structure in the vicinity of the optic disk. A fuzzy convergence algorithm was proposed to determine the intersection of the blood vessel segments [29]. The method proposed in [30] introduced a geometrical directional model of the retinal vascular tree to detect the convergence point of vessels. Youssif *et al.* [44] proposed an approach to detect the optic disk by matching the directions of the neighboring blood vessels with a vessels' direction matched filter. In [31], the entropy of vascular directions was used. The entropy is thought to be associated with the occurrence of a large number of vessels with multiple orientations. As shown in Fig. 2b, the divergent point of the main vessel tree, however, is not always exactly at the center of the optic disk. Therefore, these methods may suffer from insufficient precision in the localization of the optic disk.

The studies [39], [40], [45], [46] focused on the cup segmentation. The work in [39] proposed a spatial heuristic ensembling approach which fuses different methods to segment the cup. Later, Wong *et al.* [40] proposed a method to identify the boundary of the cup by determining the vessel

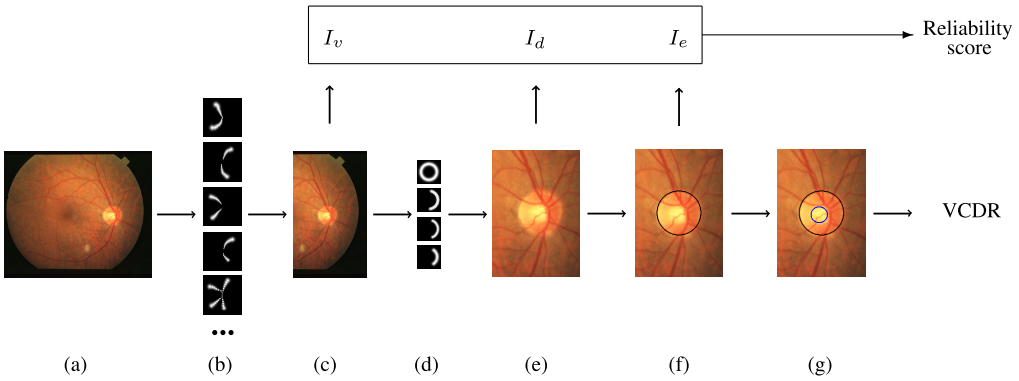

FIGURE 4. Schematic overview of the proposed approach. For a given (a) retinal fundus image we first apply (b) a set of vasculature-selective COSFIRE filters to detect the divergent point of the major vessels. Then, (c) we crop a large region around the maximum response and apply (d) a set of disk-selective COSFIRE filters to detect bright disk patterns. (e) We crop a small region around the maximum response of the disk-selective COSFIRE filters and fit an ellipse to approximate the boundary of the detected optic disk. The black boundary in (f) indicates the delineated disk boundary. We then employ generalized matrix learning vector quantization to segment the disk region into the neuroretinal rim and the cup. (g) The blue boundary inside the disk indicates the determined cup. Finally, we compute the VCDR according to the determined cup and disk and provide a reliability score.

kinking points, which indicate the cup excavation. Recently, Sevastopolsky [45] and Fu *et al.* [46] proposed joint disk and cup segmentation based on deep convolutional neural networks. Moreover, the methods proposed in [15], [18], [42], and [43] rely on the analysis of retinal fundus images to automatically assess glaucoma. The work in [42] proposed an automatic system to estimate the glaucoma risk index which indicates the probability of a retina being glaucomatous. Their system extracts features, such as FFT and *B*-spline coefficients, from the spatial and the frequency domains followed by a support vector machine classification. The work proposed in [15] and [43] implemented deep learning approaches to automatically extract discriminant features for the differentiation of the glaucomatous retinas from the healthy ones. Most of these methods were, however, tested on proprietary data sets or public data sets with ground truth data that is not publicly available.

Some other approaches [47], [48] detect the optic nerve head in stereo retinal fundus images which provide depth information or in OCT images [49]. Systems that rely on sophisticated equipment are, however, not considered suitable for population screening as they are too time consuming and require expensive resources.

III. PROPOSED METHOD

A. OVERVIEW

We propose a novel approach for assisting population-based glaucoma screening and we provide the manual annotation by an experienced ophthalmologist[2] for eight public data sets. In our approach, we first localize the optic disk by using two types of trainable COSFIRE (Combination of Shifted Filter Responses) filters [50]: one type configured to be selective for the divergent points of vessel trees and the other type configured to be selective for circular bright regions. We then fit an ellipse that approximates the boundary of the detected optic disk. Next, we apply generalized matrix learning vector quantization to segment the delineated optic disk into two regions: the cup and the neuroretinal rim. Finally, we compute the VCDR and provide a reliability score of the measurement. Fig. 4 illustrates a schematic overview of the proposed procedure.

[2]The manual annotation data can be downloaded from http://matlabserver.cs.rug.nl/.

B. LOCALIZATION OF THE OPTIC DISK

We use two types of trainable COSFIRE filters for the localization of the optic disk. First, we use a set of COSFIRE filters that are selective for divergent points of thick vessels. Such filters are automatically configured using training images as we explain below. We then consider the neighborhood of the location where we achieve the maximum response from the concerned vasculature-selective COSFIRE filters. Subsequently, we apply a set of disk-selective COSFIRE filters in order to improve the localization of the optic disk.

1) COSFIRE FILTERS

COSFIRE filters are trainable pattern detectors and have been demonstrated to be effective in various applications [51]–[57]. One type of such a filter takes as input the responses of a bank of Gabor filters that are selective for contour parts of different widths and orientations. The types of Gabor filter and the positions at which we take their responses are determined in an automatic configuration procedure. This procedure locates the local maxima responses of a bank of Gabor filters along a set of concentric circles in a prototype pattern of interest and forms a set of 4-tuples: $S = \{(\lambda_i, \theta_i, \rho_i, \phi_i) \mid i = 1 \ldots n\}$. The parameters (λ_i, θ_i) in the i-th tuple are the wavelength and the orientation of the involved Gabor filter that is selective for contour parts with thickness of (roughly) $\lambda_i/2$ pixels and orientation θ_i, while

(ρ_i, ϕ_i) are the distance and the polar angle where the local maximum response of the concerned Gabor filter is located with respect to the support center of the filter.

The response of a COSFIRE filter is then computed by combining the responses of the selected Gabor filters. In the original work, the combination is achieved by a weighted geometric mean, which responds only when every contour part of interest is present in the given pattern. COSFIRE filters are able to achieve tolerance to rotation, scale and reflection by manipulating the model parameters. We do not elaborate on this aspect and refer the interested readers to [50].

In this work, we make modifications to the application of COSFIRE filters so that they can adapt to the cases that parts of the patterns of interest are missing or occluded. We binarize the responses of Gabor filters by thresholding with a fraction ($t_1 = 0.4$) of the maximum response value and dilate (instead of blurring) each of these responses by a disk-shape structuring element[3] in order to allow for some spatial tolerance. We use the arithmetic mean (instead of the geometric mean) as the output function in order to increase the tolerance to missing contour parts in patterns of interest.

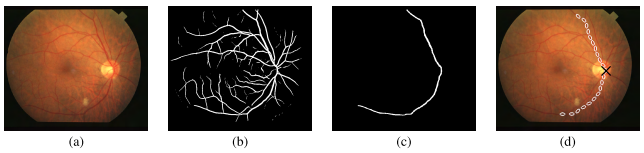

FIGURE 5. Configuration of the vasculature-selective COSFIRE filters. (a) Example of a coloured retinal fundus image (of size 605 × 700 pixels) taken from the STARE data set [29]. (b) Vessel tree delineated by the method proposed in [52]. (c) Binary image of the corresponding main vessel (of thickness 10 pixels). (d) The structure of the resulting vasculature-selective COSFIRE filter. The black cross marks the vessel divergence point and is used as the support center of the COSFIRE filter. The white ellipses illustrate the wavelengths and orientations of the selected Gabor filters and their positions indicate the locations from which the responses of these Gabor filters are taken with respect to the center.

2) CONFIGURATION OF A VASCULATURE-SELECTIVE COSFIRE FILTER

Fig. 5a shows an example of a retinal fundus image. We first extract its major vessels by the delineation algorithm proposed in [52] and then manually remove the small branches of blood vessels to obtain a binary image with only the major vessels. Fig. 5c shows the resulting vessel segmentation binary map and the corresponding major vessel tree. We use the major vessel pattern as a prototype to configure[4] a COSFIRE filter, which we denote by S_v, with the method proposed in [50]. The point from which the big vessels diverge is used as the support center of the concerned COSFIRE filter. Fig. 5d illustrates the structure of the resulting COSFIRE filter superimposed on the input image. The ellipses represent the wavelengths and the orientations of the selected Gabor filters and their positions indicate the locations at which their responses are used to compute the response of the COSFIRE filter.

[3]The radius R of the structuring element is a linear function of ρ: $R = 0.1\rho$.

[4]The parameters of the COSFIRE filter are: $\lambda = 20$, $\theta \in \{\frac{\pi i}{8} | i = 0, \ldots, 7\}$, $\rho \in \{0, 50, \ldots 500\}$, $t_1 = 0.4$.

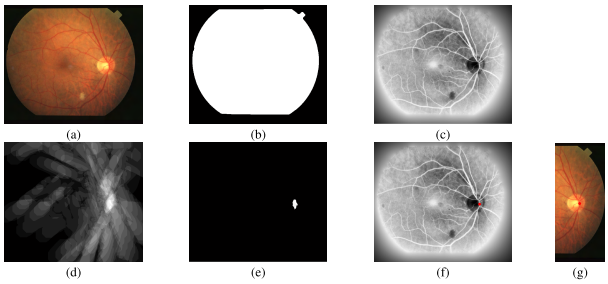

FIGURE 6. Application of a vasculature-selective COSFIRE filter. (a) Example of a colour retinal fundus image (of size 605 × 700 pixels) from the STARE data set. (b) The automatically determined FOV mask. (c) The preprocessed image. (d) The output response map of the vasculature-selective COSFIRE filter to the image in (c). (e) The thresholded response map. (f) The red dot indicates the centroid of the thresholded responses in (e). (g) The cropped retinal image (of size 605 × 231 pixels) around the detected point.

3) RESPONSE OF A VASCULATURE-SELECTIVE COSFIRE FILTER

Before applying a COSFIRE filter, we first apply a preprocessing step to the green channel of the input image in order to obtain the field-of-view (FOV) region (Fig. 6b) and enhance the contrast by histogram equalization (Fig. 6c). We elaborate on the generation of the FOV mask in Section IV-B1.

Next, we apply the configured vasculature-selective COSFIRE filter to the preprocessed retinal image. The output of the COSFIRE filter is the arithmetic mean of all the dilated and shifted Gabor filter responses that correspond to the tuples in the set S_v:

$$r_{S_v}(x, y) \stackrel{\text{def}}{=} \left| \frac{1}{n_v} \left(\sum_{i=1}^{|S_v|} s_{\lambda_i, \theta_i, \rho_i, \phi_i, \delta_i}(x, y) \right) \right|_{t_v} \quad (1)$$

where $|\cdot|_{t_v}$ stands for thresholding the output at a threshold value $t_v = 0.95$, and $s_{\lambda_i, \theta_i, \rho_i, \phi_i, \delta_i}(x, y)$ is the dilated and shifted Gabor filter response in location (x, y) with parameter values specified in the i-th tuple. We specify how to obtain the value of the threshold parameter t_v in a training phase that we describe in Section IV-C1. Fig. 6d shows the response map of the filter and Fig. 6e illustrates the thresholded response map. Finally, we consider the centroid of the thresholded output (Fig. 6f) as the center and crop a rectangular region around the center (Fig. 6g).

4) LOCALIZATION OF THE OPTIC DISK

So far we demonstrated how we apply a vasculature-selective COSFIRE filter to (approximately) determine the position of the optic disk. Here, we explain how we localize the optic disk more precisely by detecting the bright disk region. Similar to vessel divergence detection, we use COSFIRE filters but this time they are selective for disk-shaped patterns. Empirical experiences show that this approach is much more robust to noise than the Circular Hough Transform [58].

FIGURE 7. Configuration of a COSFIRE filter that is selective for a bright disk. (a) A synthetic input image (of size 150 × 150 pixels) that contains a bright disk of radius 50 pixels. (b) The superposition of the responses of a bank of anti-symmetric Gabor filters with a wavelength $\lambda = 30$ pixels and eight orientations $\theta \in \{\frac{\pi i}{8} \mid i = 0...7\}$). (c) The structure of the resulting COSFIRE filter.

We use a synthetic disk image shown in Fig. 7a as a prototype pattern to configure a COSFIRE filter. We implement the same configuration procedure[5] as proposed for the vasculature-selective COSFIRE filter. We use anti-symmetric Gabor filters that respond to edges (with a wavelength $\lambda = 30$ pixels and eight orientations $\theta \in \{\frac{\pi i}{8} \mid i = 0...7\}$).

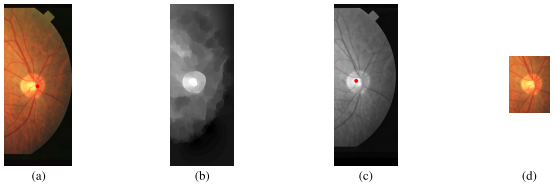

FIGURE 8. Application of a disk-selective COSFIRE filter. (a) The input image is the automatically cropped part of a retinal image (of size 605 × 231 pixels) resulting from the localization step. (b) Preprocessed image of the cropped area. (c) The red dot indicates the location at which the maximum response of the COSFIRE filter is achieved. (d) The resulting cropped area (of size 209 × 153 pixels) around the detected point.

Before we apply the disk-selective COSFIRE filter, we first preprocess the automatically cropped input image that contains the optic disk, Fig. 8a. The preprocessing steps consist of vessel segmentation and inpainting of vessel pixels (details provided in Section IV-B2) as well as edge preserving smoothing [59]. The resulting preprocessed image is shown in Fig. 8b. The red spot in Fig. 8c indicates the position at which we achieve the maximum COSFIRE filter response, and we use it to indicate the center of the optic disk. We then crop a small rectangular region from the original image around the detected point, Fig. 8d.

C. DELINEATION OF THE OPTIC DISK BOUNDARY

Fig. 9a shows an automatically cropped image containing the optic disk and Fig. 9b illustrates the result of the vessel segmentation and inpainting. We delineate the optic disk boundary by computing the best fit of an ellipse to the cropped region obtained above. Then we compute the smoothed x- and y-partial derivatives. This is achieved by convolving the preprocessed image in Fig. 9b with the two partial first order derivatives of a 2D Gaussian function (with a standard deviation of $\sqrt{2}$). Fig. 9(c-d) show the corresponding

[5]The parameters for the disk-selective filter: $\lambda = 30$, $\theta \in \{\frac{\pi i}{8} \mid i = 0...7\}$, $\rho = 50$, $t_1 = 0.81$.

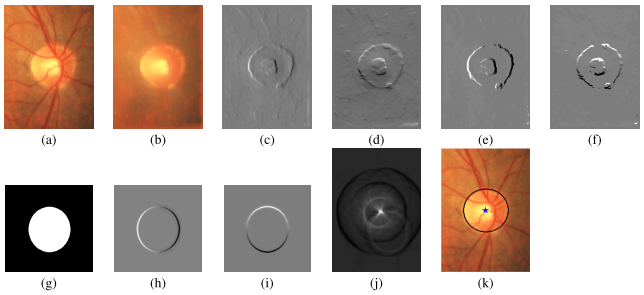

FIGURE 9. Delineation of the optic disk boundary. (a) An optic disk image (of size 209×152 pixels) cropped automatically from a retinal fundus image in the localization step. (b) Result of the preprocessing of the cropped region. (c-d) The x- and y- derivative maps, and their (e-f) enhanced versions. (g) Synthetic disk image (of size 150 × 150 pixels). (h-i) The x- and y-derivative maps of the synthetic disk in (g). (j) The sum of correlations between the partial derivatives of the preprocessed disk image and a synthetic ellipse that best fits the concerned optic disk. (k) The black ellipse indicates the best delineation of the optic disk with the horizontal and vertical axes of size 73 and 70 pixels, respectively. The blue star marker indicates the location of the maximum correlation sum response, and we consider this point to be the center of the optic disk.

derivative maps. We change to unit length all gradient vectors of magnitude larger than or equal to 0.2 of the maximum gradient magnitude across the image. The idea of this operation is to make the responses along the boundary of the optic disk similar to the responses to a synthetic ellipse of uniform intensity - compare Fig. 9e with Fig. 9h and Fig. 9f with Fig. 9i.

Subsequently, we correlate the two enhanced derivative maps, Fig. 9(e-f), with a pair of derivative maps of a synthetic ellipse, Fig. 9(h-i), and sum up the output maps of the respective two correlations. We repeat this procedure for ellipses of different radii and ellipticities and we determine the semi axes of the synthetic ellipse that yields the maximum sum of correlations. Fig. 9j shows the sum of correlations between the partial derivatives of the preprocessed disk image and a synthetic ellipse that best fits the concerned optic disk. The location at which the maximum sum is obtained is used to represent the center of the optic disk. The black boundary in Fig. 9k is the ellipse that gives the highest correlation result.

D. DETERMINATION OF THE CUP REGION

The boundaries of the cup are typically diffuse and they are often occluded by blood vessels. Thus, the edge-based approaches are not sufficiently robust for the segmentation of the cup. Therefore, we apply a supervised classification approach called Generalized Matrix Learning Vector Quantization (GMLVQ) [23] for the detection of the cup.

Learning Vector quantization (LVQ) [60] is a prototype-based classification approach that performs distance learning to optimize the discrimination of classes. An LVQ classifier is represented by prototypes which are learned in the feature space of the training data. The classification is performed by a winner-takes-all scheme, in which a new data sample is classified to the class given of the nearest prototype. The GMLVQ model extends the distance measure with an

adaptive relevance matrix that ranks the importance of single features and their combinations for the categorization tasks. For the detailed information about the mathematical explanation of the GMLVQ classifier, we refer to the work in [23]. We use the public available toolbox provided in [61] for the implementation and all other parameters were set as the default values [61]. For the pixel-wised classification of the neuroretinal rim and the cup, we consider two prototypes for the neuroretinal class and one for the cup class. We form the pixel wise feature vector with seven elements, namely the Red, Green, Blue, Hue, Saturation and Lightness from the RGB and HSV colour spaces as well as the distance of each pixel with respect to the center of the optic disk. We use half of the images from each data set to train the classifiers and the rest as the test images. Fig. 10a shows ans example of the determined cup/rim region with GMLVQ.

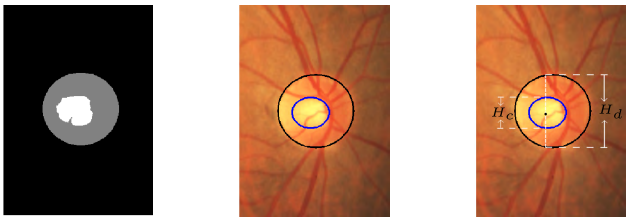

FIGURE 10. Computation of the VCDR value. (a) Result of the cup detection from the GMLVQ. (b) The final determined cup which is indicated by the inner ellipse in blue. (c) Computation of the VCDR. The black dot indicates the center of the cup. The VCDR here is equal to 0.41.

Next, we use morphological closing followed by an opening to connect the isolated regions and remove small islands. The empirical sizes of the disk-shaped structuring elements for these morphological operations are fractions of 0.1 and 0.05 of the maximum axis of the determined optic disk, respectively. We then fit an ellipse to the white region with its center being the center of mass and its vertical and horizontal axes being the height and width of the concerned component, respectively. The blue ellipse in Fig. 10b illustrates the cup region.

E. VERTICAL CUP-TO-DISK RATIO (VCDR)

We compute the VCDR as the ratio $\frac{H_c}{H_d}$ of the height of the ellipse representing the cup H_c and the height of the delineated disk H_d with respect to the center of the cup. For the considered example in Fig. 10c, the VCDR is 0.41.

IV. IMPLEMENTATION AND EXPERIMENTAL RESULTS

A. DATA SETS

We experiment on nine public data sets of retinal fundus images, which are listed in Table 1. These data sets contain a total of 2109 images of different sizes and FOV angles. Most of them were originally created for the purpose of vessel segmentation or diabetic retinopathy screening. Among these data sets, only the DRISHTI-GS1 data set [62] has annotations of glaucoma-related features, namely boundaries

TABLE 1. List of public data sets[6] in alphabetical order.

Data set	No. of images	Image size (pixels)	FOV
CHASEDB1 [66]	28	999×960	30°
DIARETDB1 [67]	89	1500×1150	50°
DRISHTI-GS1 [62]	101	2049×1751	30°
DRIONS [63]	110	600×400	30°
DRIVE [11]	40	565×584	45°
HRF [65]	45	3504×2336	60°
MESSIDOR [68]	1200	2240×1488	45°
ONHSD [64]	99	760×570	45°
STARE [29]	397	700×605	-

of the optic disks and the cups. The DRIONS [63] and the ONHSD [64] data sets provide annotations of the optic disk boundaries and the HRF data set [65] gives the centers of the optic disks. None of the other data sets provide any annotations of glaucoma-related features.

One of our contributions in this work is the annotation[7] of the optic disk and the cup boundary points for the first eight data sets made by an experienced ophthalmologist from the University Medical Center Groningen (UMCG). He used an annotation tool to mark the leftmost, the rightmost, the topmost and the bottommost boundary points of the optic disk as well as those of the cup in each image. Fig. 11 shows some examples of the manual annotations. We then fit two ellipses to these eight points to represent the annotated boundaries of the optic disk and the cup in each image, from which we can compute the groundtruth cup-to-disk ratios.

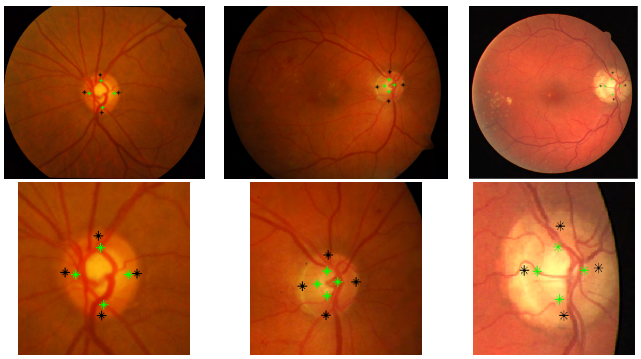

FIGURE 11. Examples of manual annotations of optic disks and cups in retinal fundus images (taken from the DRISHTI-GS1, DIARETDB1 and the DRIVE data sets, respectively) by the ophthalmologist. The black stars indicate the boundary points of the optic disks while the green stars are the boundary points of the cups. The bottom row shows the close-up views of these examples.

In our experiments, we use all 397 images in the STARE data set to configure vasculature-selective COSFIRE filters. We evaluate the proposed approach on all 850 test images in the other eight data sets.

[6]DRIONS, HRF and STARE data sets do not provide the FOV angle. Since the images in the DRIONS and HRF data sets were obtained with the same FOV angles, we randomly selected some images from each data set and measured manually their FOV angles. The FOV angles, however, vary a lot in the STARE data set.

[7]These annotations (specifications of the optic disk and cup boundaries) can be downloaded from http://matlabserver.cs.rug.nl.

B. PRE-PROCESSING PROCEDURES

Here, we elaborate on the pre-processing steps that we mentioned briefly in Section III.

1) IMAGE RESCALING AND FOV MASK GENERATION

In order to keep fixed parameters of the proposed method, we resize every image in such a way that the FOV region has a diameter of 1024 pixels.

Since not every data set provides the FOV masks, we generate them by binarizing the grayscale versions of the RGB images with thresholds that we determine automatically as follows. We sort in ascending order the intensity values of all pixels in each image. Then we compute the first order derivative of this one-dimensional array and set the threshold to be the intensity value, at which the first order derivative is maximum. This design decision is motivated by the fact that the background pixels have relatively small (close to 0) intensity values, which arise a high first order derivative at the transition to the pixels within the FOV region. After the binarization, we apply morphological closing with a disk-shaped structuring element of radius 20 pixels to obtain the FOV mask as one connected component.

2) VESSEL EXTRACTION AND IMAGE INPAINTING

We extract blood vessels by the method proposed in [52]. We use the online implementation with the parameters tuned for the detection of thick blood vessels.[8] Next, we use the inpainting algorithm proposed in [69] that fills in the removed vessel pixels with the intensity values that are interpolated from the neighboring pixels.

3) PRE-ESTIMATION OF THE OPTIC DISK WIDTH

The pre-estimation of the optic disk width is important for the accurate localization and segmentation of the optic disk. In retinal fundus images, some features, such as blood vessels, myelinated optic nerves and hard exudates, may interfere with the accurate detection of the optic disk. These features usually contain curvatures that are similar in shape to the boundaries of the optic disk. By pre-estimating the size of the optic disk, we are able to rule out these interferences and improve the accuracy of the disk detection while reducing the computation time needed to search for the best approximating ellipse.

The epidemiologic investigation in glaucoma [70] has shown that the viewing angle of the optic disk ψ_{disk} is roughly between 4° and 9°. We use this finding and denote by γ the set of pre-estimated widths of the optic disk in pixels:

$$\gamma = \{1024\psi_{disk}/\psi_{im} \mid \psi_{disk} = 4, 4.1, \ldots, 9\}$$

where 1024 is the diameter of the FOV region of an image and ψ_{im} is the viewing angle of that image. For instance, the retinal fundus images in the CHASEDB1 data set[9] captured with an FOV angle of (ψ_{im} =) 30° have optic disk diameters ranging from (1024 × 4/30 =) 137 to (1024 × 9/30 =) 307 pixels. For the images of unknown FOV angle, we assume it to be 45°, as it is the most commonly used FOV angle.

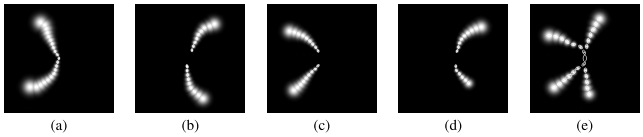

FIGURE 12. The structures of five examples of vasculature-selective COSFIRE filters. The white ellipses illustrate the wavelengths and orientations of the selected Gabor filters and their positions indicate the locations where the responses of these Gabor filters are taken with respect to the support center of the COSFIRE filter. The bright blobs represent the dilation operations (see Section III-B1) that provide some spatial tolerance.

C. IMPLEMENTATION OF THE PROPOSED APPROACH

1) CONFIGURATION OF VASCULATURE- AND DISK-SELECTIVE COSFIRE FILTERS

For the configuration of vasculature-selective COSFIRE filters, we randomly select a retinal fundus image from the training set, i.e. the STARE set, and generate its binary vessel pattern image as the one shown in Fig. 5c. Next, we use the resulting binary vessel pattern as a prototype to configure a vasculature-selective COSFIRE filter as described in Section III-B2. We then apply the resulting filter with reflection invariance to all images in the training set. We set the threshold value t_v such that it yields no false positives. For the COSFIRE filter configured with the pattern in Fig. 5c, the threshold parameter t_v is set to 0.96. This filter correctly detects the vessel divergent points in 35 training images. Fig. 12a illustrates the structure of the resulting COSFIRE filter, which we denote by S_{v_1}. For the configuration of this filter, we use the set of radii values $\rho \in \{0, 50, .., 500\}$. For the remaining images whose vessel divergent points are not detected by the filter S_{v_1}, we perform the following steps. We randomly select one of these training images and use its binary vessel pattern to configure a new filter S_{v_2}. Then we apply this filter to the training images that were missed by the first filter and determine its threshold value. We repeat this procedure of configuring filters until the divergent points of all training images are detected. For the STARE data set with 397 images as our training set, we need 27 vasculature-selective COSFIRE filters. Fig. 12 shows some examples of the structures of such filters. We apply in sequence the 27 vasculature-selective COSFIRE filters as described in Section III-B3. A response of a vasculature-selective COSFIRE filter indicates the presence of a vessel tree. As soon as one of the 27 filters responds sufficiently

[8] We use only symmetric filters with parameters: $\sigma = \{2.1, 5.2, 10.4, 15.6\}$, $\rho = \{0, 5, 10, \ldots, 20\}$, $\sigma_0 = 3$ and $\alpha = 0.6$.

[9] The images in the CHASEDB1 data set are all rescaled to 1093 × 1137 pixels, while the widths of the FOV region of the images are rescaled to 1024 pixels.

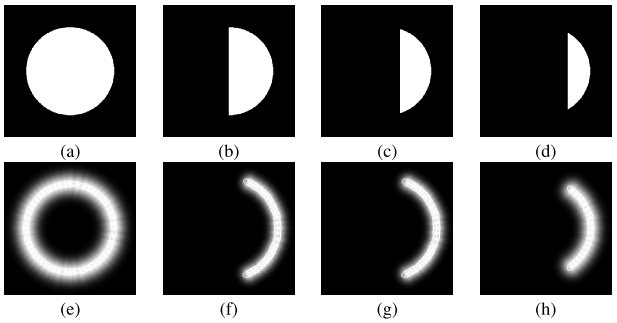

FIGURE 13. (Top row) Synthetic patterns and (bottom row) the structures of the resulting disk-selective COSFIRE filters.

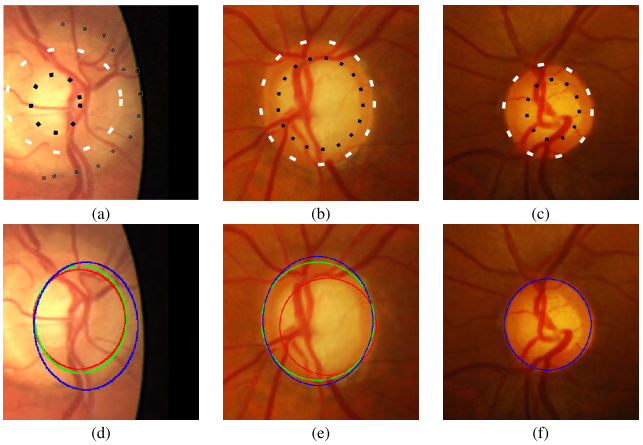

FIGURE 14. Examples of the optic disk regions cropped from the retinal fundus images as well as their corresponding delineation results. (a) An optic disk with surrounding parapapillary atrophy. (b-c) Optic disks with with a larger, bright cup. The white dashed lines indicate the boundaries of the optic disks. The black dashed lines inside the optic disks are the boundaries of the cups while the outer one in (a) indicates parapapillary atrophy. (d-f) The corresponding results of the disk delineation. The red, green and blue ellipses indicate the best fits from the three ranges of considered widths. The three ellipses overlap each other in (f) leaving only the blue one visible.

to the given image, we stop applying the remaining ones. We denote by I_v a reliability indicator of this detection; it is equal to 1 when there is a filter that responds to the image, otherwise it is 0.

For the configuration of disk-selective COSFIRE filters, we use the four synthetic images in the top row of Fig. 13 as prototype patterns. The three patterns in Fig. 13(b-d) have areas that cover 50%, 40% and 30% of the disk in Fig. 13a, respectively. We show the corresponding structures of the disk-selective COSFIRE filters in the bottom row. We denote by S_{c_1}, S_{c_2}, S_{c_3} and S_{c_4} the four disk-selective COSFIRE filters which have empirically determined threshold values $t_v(S_{c_1}) = 0.81$, $t_v(S_{c_2}) = 0.95$, $t_v(S_{c_3}) = 1$, $t_v(S_{c_4}) = 1$. The last three filters are used to detect the optic disks which have part of the disk boundaries missing. They (Fig. 13(c-d)) contain only 30%-40% of the boundary of a complete disk. We configure a family of disk-selective COSFIRE filters by using synthetic circles whose radii increase in intervals of 10 pixels from the minimum to the maximum pre-estimated widths of the optic disk. For each radius in this range we configure four COSFIRE filters of the type described above. Similar to the way we apply the vascular-selective filters, we apply in sequence all the configured disk-selective COSFIRE filters. We denote by I_d the reliability indicator of the bright disk, which is 1 when one of the disk-selective filters responds, otherwise 0.

2) DISK DELINEATION

As shown in Fig. 14(a-c), it is common to have the PPA and a bright cup in the vicinity of the optic disk, which may disturb the accurate delineation of the optic disk. PPA and the cups have a bigger and smaller diameter than that of the optic disk, respectively. In order to address this challenge, we group the set of pre-estimated widths γ of the optic disks into three ranges, which contain the first 60%, 80% and 100% of the values of γ. For each range, we select the ellipse that best delineates the disk boundary as described in Section III-C. In this way, we end up with three ellipses, as shown in Fig. 14(d-f). The red, green and blue ellipses represent the best ellipses determined from the considered three ranges of widths. We then compute the similarity between every pair of the ellipses as follows. We calculate the distances between their center locations and the sum of the absolute differences between their widths and heights. Only if both values are smaller than 10 pixels, we consider such a pair of ellipses as similar, otherwise we treat them as different. We denote by I_e a reliability indicator that concerns the delineation of the disk boundary. It can have one of four values (0, 1/3, 2/3, or 1) that represents the proportion of the number of similar ellipses. Finally, we determine the center, width and height of the optic disk as the mean values of the locations, widths and heights of the three ellipses. For the case that only two ellipses are similar, we take the mean of the locations, widths and heights of the two ellipses. For the example shown in Fig. 14d, the final disk boundary is approximated by the ellipse determined from the mean of the red and green ellipses. Fig. 14e has the delineated disk boundary coming from the mean of the green and the blue ellipses and the disk boundary in Fig. 14f is the mean of the three ellipses.

D. EXPERIMENTAL RESULTS

We evaluate the performance of the proposed approach on the following aspects: disk localization, disk height error, cup height error and VCDR values.

1) PERFORMANCE OF THE OPTIC DISK LOCALIZATION

We compare the automatically obtained results with the ones provided by an experienced ophthalmologist. As suggested in [29] for the evaluation of the localization step, we consider the location of the optic disk is correct if the center of the detected optic disk is located inside the manually identified one in the ophthalmologist annotation. We then compute

TABLE 2. Localization accuracy (%) and average localization error (δ_L) of the proposed approach on all images in the eight data sets comparing to a recently published approach proposed in [71].

Data set	Our method (δ_L)	Akram et al [71](%)
CHASEDB1	96.43 (0.09)	-
DIARETDB1	98.88 (0.05)	100
DRISHTI-GS1	99.01 (0.04)	-
DRIONS	100 (0.05)	100
DRIVE	97.50 (0.08)	100
HRF	97.78 (0.10)	100
MESSIDOR	99.08 (0.06)	98.91
ONHSD	91.92 (0.07)	-
Weighted mean	98.54 (0.06)	99.11

TABLE 3. Performance measurements of the disk height (δ_D) and the cup height (δ_C) on the test data sets. We mark in bold the best result for the measurements.

Data set	δ_D	δ_C
CHASEDB1	0.11	0.11
DIARETDB1	0.08	0.08
DRISHTI-GS1	0.08	0.07
DRIONS	0.09	0.11
DRIVE	0.09	0.08
HRF	**0.07**	**0.06**
MESSIDOR	0.08	0.10
ONHSD	0.09	0.16
Weighted mean	0.08	0.09

TABLE 4. VCDR errors on the test data sets. We mark in bold the best result for the measurement.

Data set	VCDR error
CHASEDB1	**0.06**
DIARETDB1	0.12
DRISHTI-GS1	0.16
DRIONS	0.13
DRIVE	0.08
HRF	0.17
MESSIDOR	0.11
ONHSD	0.13
Weighted mean	0.11

the relative error of the optic disk localization, which is the distance between the automatically determined disk center and the one from the manual annotation divided by the height of the disk in the manual annotation. We report the results of the localization accuracy and the average localization error in Table 2.

2) PERFORMANCE OF THE HEIGHT ESTIMATION OF THE OPTIC DISK AND THE CUP

We evaluate the performance of the height estimation of the optic disk and the cup by the relative height error (RHE). We report the results in Table 3.

$$RHE = \frac{|HD - HG|}{HG},$$

where HD is the height of the detected disk or cup while HG is the corresponding height from the manual annotation.

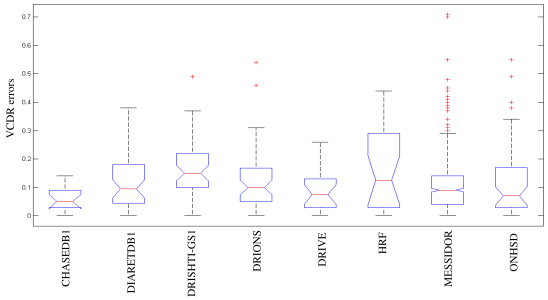

FIGURE 15. Box-whisker plot of the VCDR errors on all test images in each data set.

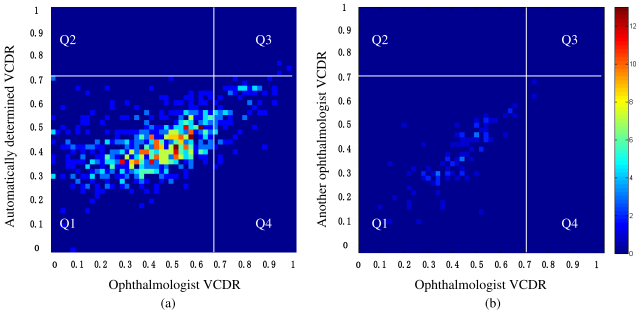

FIGURE 16. Distributions of the obtained VCDR values. (a) Distribution of the automatically obtained VCDR values on images with respect to the manual annotation from the ophthalmologist. The x-axis represents the VCDR values provided by the ophthalmologist while the y-axis represents the automatically obtained VCDR values. (b) Distribution of the VCDR values provided by another ophthalmologist with respect to the manual annotation from the ophthalmologist. The x-axis represents the VCDR values provided by the ophthalmologist while the y-axis is the VCDR values provided by the second observer. The intensity values in both matrices indicate the number of images falling in the grid regions. The vertical line represents the decision threshold $VCDR^{oph}$ of the image label, which is set to 0.7, while the horizontal line is the classification of the images by the automatic system. The ones that fall into Q1, Q2, Q3 and Q4 areas are the true negatives, false positives, true positives and false negatives, respectively. The sensitivity is computed as $\frac{\#Q3}{\#Q3+\#Q4}$ while the specificity is $\frac{\#Q1}{\#Q1+\#Q2}$, where # indicates the number of images falling in the region.

3) PERFORMANCE OF VCDR ESTIMATION

Next, we compute the errors of the automatically obtained VCDR values with respect to those from the manual annotations by the ophthalmologist. Fig. 15 illustrates the box and whisker diagrams of the VCDR errors for all 850 test images, which show the distribution of the errors in each data set. As we see from the plots, the median values of the VCDR errors are around 0.1, which are indicated by the red horizontal lines. In Fig. 16a, we illustrate the distribution of the obtained VCDR values in all test data sets with respect to the manual annotation of the ophthalmologist. Fig. 16b shows the inter-observer variability between two ophthalmologists on 100 randomly selected images. We also illustrate in Fig. 17 the Bland-Altman plot of the automatically determined VCDR values with respect to the manual annotation from the ophthalmologist. Such a plot is used to analyze the

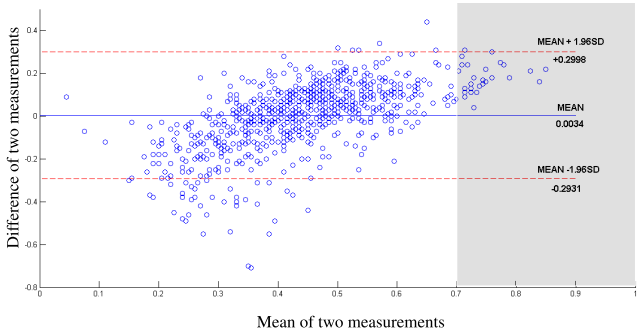

FIGURE 17. Bland-Altman plot of the automatically determined VCDR values with respect to the manual annotation from the ophthalmologist. The *x*-axis and the *y*-axis of the plot are the mean and the difference of the VCDR values obtained from the proposed approach and the ophthalmologist, respectively. Each blue circle represents an image and the blue line indicates the mean value while the red dashed lines indicate the mean value ±1.96 times the standard deviation. The images falling in the shaded area concern VCDR values above the 97.5^{th} percentile of the general population (indicating pathology).

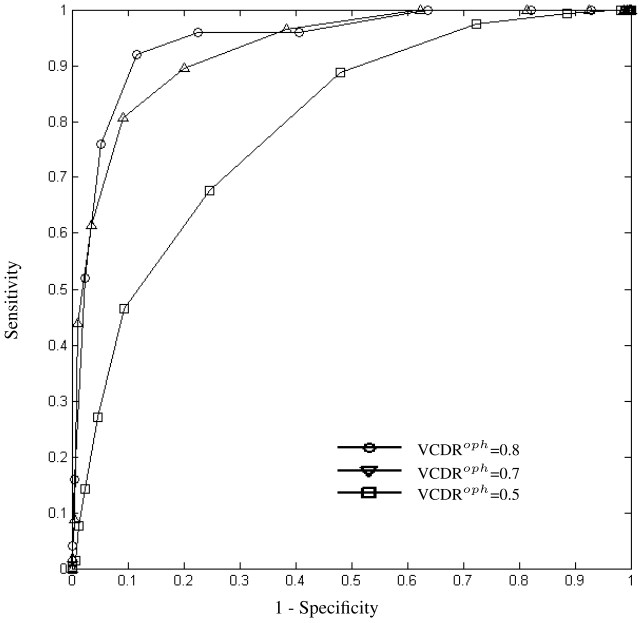

FIGURE 18. ROC curves of the automatically obtained VCDR values with respect to the manual annotation provided by the ophthalmologist. We obtain these curves by ranging the VCDR* threshold between 0 and 1 in intervals of 0.05. The area under the curve (AUC) is equal to 0.79, 0.93 and 0.94 when we set the $VCDR^{oph}$ to 0.5, 0.7 and 0.8, respectively.

agreement between two measurements. The mean difference (bias) between the automatically obtained VCDRs and those from the ophthalmologist was −0.0034 and the mean difference plus/minus 1.96 times the standard deviation (limits of agreement) were +0.30 and −0.29, respectively. For the inter-observer variability (Fig. 16b), these values were 0.03, 0.19, and −0.13, respectively. As indicated by the shaded region in Fig. 17, the proposed approach achieved a much better agreement (smaller difference) on images with a large VCDR (>0.7) according to the manual annotations. This is important, because a VCDR above 0.7 indicates pathology.

4) PERFORMANCE OF THE CLASSIFICATION OF GLAUCOMATOUS RETINAS

In clinical practice, glaucoma experts do not rely on a VCDR value alone to conclude whether a patient has glaucoma or not. However, the automatic computation of VCDR can be highly beneficial to experts as it can be used to decide much quicker whether other checks are necessary or not. In order to get an indication of the screening performance of our method, we computed the sensitivity and specificity. We used $VCDR^{oph} = 0.7$ as a threshold to label the images as healthy or glaucomatous (corresponding to the 97.5^{th} percentile of the general population [14]). We then took a threshold value denoted by VCDR* and vary it between 0 and 1. We compute the sensitivity and specificity and illustrate it in Fig. 18. This figure shows the receiver operating characteristic (ROC) curve of the automatic method. The closer such a curve is to the top-left corner, the better the performance of the approach is. In the same way, we obtained ROC curves for threshold $VCDR^{oph}$ equal to 0.5 and 0.8 (presented in the same figure). We achieved an area under the curve (AUC) of 0.79, 0.93 and 0.94 for $VCDR^{oph}$ equal to 0.5, 0.7, and 0.8, respectively.

V. DISCUSSION

We propose a systematic approach that computes the VCDR to assist ophthalmologists in population-based glaucoma screening. We experimented on eight public data sets with a total of 1712 retinal fundus images and evaluated the performance of the approach. We compared the localization performance of our method with a recently published approach proposed in [71] and reported comparable results in Table 2. In our work we provided further results on three other data sets that were not used in [71], including the DRISHTI-GS1 data set that contains retinal images with a high number of glaucomatous cases and the ONHSD data set that has many images taken under insufficient illumination. The images whose optic disks are not correctly localized in the DIARETDB1, DRIVE and HRF data sets were later indicated as unreliable cases by the proposed reliability score. In Fig. 19, we show the four images from the DRIVE data set that our algorithm labeled as unreliable as well as the segmentation results. The first image is marked as unreliable due to the uncertain presence of the optic disk pattern. The problems of the other three images are due to the presence of PPA outside the disk boundaries.

In the evaluation of the optic disk and cup height determination we achieved a mean relative height error of 0.08 and 0.09, respectively. For the evaluation of the VCDR values, we achieved a mean VCDR error of 0.11 on 850 test images. An indirect comparison is possible with several studies that proposed an automatic calculation of VCDR.

TABLE 5. Comparison of the VCDR error between the proposed approach and existing approaches on the VCDR error.

Method	VCDR error	Data sets	Availabilty of manual annotations
Mittapalli et al [41]	0.13	40 private, 19 public	No
Ayub et al [72]	0.14	100 Private	No
Septiarini et al [73]	0.04	68 Private	No
Proposed approach	**0.11**	**850 public**	**Yes**

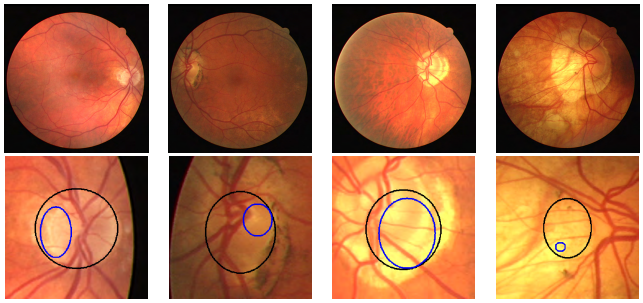

FIGURE 19. (Top row) The four retinal fundus images ('07_test.tif', '26_training.tif', '31_training.tif' and '34_training.tif') from the DRIVE data set that are indicated as unreliable. (Bottom row) The corresponding close-up views of the segmented optic disks and the cups. The black ellipses indicate the delineated optic disks while the blue ellipses are the cups. The reliability indicators (I_v, I_d, I_e) of the four images are (1,0,0.33),(1,1,0),(1,1,0) and (1,1,0), respectively. The presence of PPA is the main reason for the unreliable results.

FIGURE 20. Example of the cup segmentation from the ophthalmologist and the proposed approach on a unobvious cup excavation case. (a) An example of a retinal fundus image of unobvious cup excavation. (b) The manual segmentation of the optic disk and the cup obtained from the eight boundary points provided by the ophthalmologist. (c) The automated segmentation.

We provide a comparison of the VCDR error between our approach and existing approaches in Table 5.

The VCDR error results show that there is still room for improvement and this could be on the cup determination since most of the normal retinal fundus images do not have an obvious cup excavation. We show an example in Fig.20a. In such cases it is difficult for the proposed system to determine the cup region as indicated by the ophthalmologist (Fig.20b). This is mainly due to the fact that the pixels (except the vessel pixels) in the disk region have similar intensity values (Fig.20c). In future, we aim to investigate other segmentation algorithms that can deal with such challenging images.

In healthy eyes, the VCDR ranges from 0 to approximately 0.7 (97.5^{th} percentile [14]); in glaucomatous eyes from approximately 0.5 to - ultimately - 1.0 [21]. The agreement between our approach and the annotation of the ophthalmologist was best for VCDRs above 0.7 (Fig.17, and - related to that - our approach was able to detect VCDRs above 0.7 and especially above 0.8 with a reasonable sensitivity and specificity (Fig. 18). Fortunately, the greater VCDRs are the relevant ones to detect from the point of view of preventing blindness. For screening, a high specificity is the most important issue [74], [75]. Hence, the left part of the ROC curve (Fig.18) is the most important part.

The vasculature-selective COSFIRE filters are effective to determine the side at which the optic disk is located. In order to improve the localization precision, we applied a set of disk-selective COSFIRE filters within the selected region. The proposed two-stage localization process turned out to be essential to reduce the number of false detections. Any bright lesions, such as hard exudates, would affect the performance of disk-selective filters if they had to be applied to the entire image.

From the training set with 397 retinal fundus images, we configured 27 vasculature-selective COSFIRE filters with which we were able to detect most of the vessel trees in all retinal fundus images from the other eight data sets. By using different training and test sets, we demonstrated the robustness of the configured filters. We made all 27 filters publicly available.[10]

One of the contributions of this work is the manual annotation data of 1712 images from eight data sets, which we made available online.[11] The manual annotation was done by a glaucoma specialist at the UMCG hospital in Groningen, who marked the locations of the topmost, the bottommost, the leftmost and the rightmost boundaries of both the optic disk and the cup of all images. A randomly selected subset has been annotated by another ophthalmologist, showing a very small bias and inter-observer variability (Fig. 16b).

VI. SUMMARY AND CONCLUSIONS

We propose a novel approach for the detection of glaucoma-related features from fundus photographs. The proposed system could be deployed as part of a population-based glaucoma screening to provide effective markers and indications of retinal abnormalities. It consists of four steps, namely optic disk localization, optic disk delineation, cup delineation, and computation of the vertical cup-to-disk ratio (VCDR). For a total number of 850 test images from eight data sets we achieve a mean VCDR difference of 0.11 with respect to a glaucoma expert. Bland-Altman analysis showed that the system achieves better agreement with respect to the manual annotations for large VCDRs, which indicate pathology.

[10]The configured filters can be downloaded from http://matlabserver.cs.rug.nl.

[11]The manual annotation data can be downloaded from: http://matlabserver.cs.rug.nl.

We achieved an AUC of 0.93 for a manually annotated VCDR of 0.7 as a cut-off for pathology. We made available online the manual annotations by an experienced ophthalmologist of eight benchmark data sets in order to facilitate comparison of future methods and thus further this field.

REFERENCES

[1] H. A. Quigley and A. T. Broman, "The number of people with glaucoma worldwide in 2010 and 2020," *Brit. J. Ophthalmol.*, vol. 90, no. 3, pp. 262–267, 2006.

[2] Y.-C. Tham, X. Li, T. Y. Wong, H. A. Quigley, T. Aung, and C.-Y. Cheng, "Global prevalence of glaucoma and projections of glaucoma burden through 2040: A systematic review and meta-analysis," *Ophthalmology*, vol. 121, no. 11, pp. 2081–2090, 2014.

[3] S. C. Lin *et al.*, "Optic nerve head and retinal nerve fiber layer analysis: A report by the american academy of ophthalmology," *Ophthalmology*, vol. 114, no. 10, pp. 1937–1949, 2007.

[4] C. G. Krader. *Fundus Photography Still a Valuable Tool in Glaucoma Care*. Accessed: Apr. 15, 2013. [Online]. Available: http://ophthalmologytimes.modernmedicine.com/ophthalmologytimes/news/tags/glaucoma-360/fundus-photography-still-valuable-tool-glaucoma-care

[5] M. A. Ikram *et al.*, "The rotterdam study: 2018 update on objectives, design and main results," *Eur. J. Epidemiol.*, vol. 32, no. 9, pp. 807–850, 2017.

[6] U. Höhn *et al.*, "The ophthalmic branch of the gutenberg health study: Study design, cohort profile and self-reported diseases," *PLoS ONE*, vol. 10, no. 3, pp. 1–15, 03 2015.

[7] M. C. Leske, A. M. S. Connell, A. P. Schachat, and L. Hyman, "The barbados eye study: Prevalence of open angle glaucoma," *Arch. Ophthalmol.*, vol. 112, no. 6, pp. 821–829, 1994.

[8] L. Xu *et al.*, "Causes of blindness and visual impairment in urban and rural areas in Beijing: The Beijing eye study," *Ophthalmology*, vol. 113, no. 7, pp. 1134.e1–1134.e11, 2006.

[9] A. P. Khawaja *et al.*, "The EPIC-norfolk eye study: Rationale, methods and a cross-sectional analysis of visual impairment in a population-based cohort," *BMJ Open*, vol. 3, no. 3, p. e002684, 2013.

[10] B. E. Klein *et al.*, "Prevalence of glaucoma: The Beaver Dam eye study," *Ophthalmology*, vol. 99, no. 10, pp. 1499–1504, 1992.

[11] J. Staal, M. D. Abramoff, M. Niemeijer, M. A. Viergever, and B. van Ginneken, "Ridge-based vessel segmentation in color images of the retina," *IEEE Trans. Med. Imag.*, vol. 23, no. 4, pp. 501–509, Apr. 2004.

[12] J. Jonas, W. Budde, and S. Panda-Jonas, "Ophthalmoscopic evaluation of the optic nerve head," *Surv. Ophthalmol.*, vol. 43, no. 4, pp. 193–320, 1999.

[13] R. Weinreb and E. Greve, *Glaucoma Diagnosis: Structure and Function*. The Hague, The Netherlands: Kugler Publications, 2004.

[14] R. C. W. Wolfs *et al.*, "Changing views on open-angle glaucoma: Definitions and prevalences—The rotterdam study," *Invest. Ophthalmol. Vis. Sci.*, vol. 41, no. 11, pp. 3309–3321, 2000.

[15] X. Chen, Y. Xu, D. W. K. Wong, T. Y. Wong, and J. Liu, "Glaucoma detection based on deep convolutional neural network," in *Proc. 37th Annu. Int. Conf. IEEE Eng. Med. Biol. Soc. (EMBC)*, Aug. 2015, pp. 715–718.

[16] S. Ceccon, D. F. Garway-Heath, D. P. Crabb, and A. Tucker, "Exploring early glaucoma and the visual field test: Classification and clustering using Bayesian networks," *IEEE J. Biomed. Health Inform.*, vol. 18, no. 3, pp. 1008–1014, May 2014.

[17] P. Y. Kim *et al.*, "Novel fractal feature-based multiclass glaucoma detection and progression prediction," *IEEE J. Biomed. Health Inform.*, vol. 17, no. 2, pp. 269–276, Mar. 2013.

[18] R. G. Ramani, S. Sugirtharani, and B. Lakshmi, "Automatic detection of glaucoma in retinal fundus images through image processing and data mining techniques," *Int. J. Comput. Appl.*, vol. 166, no. 8, pp. 38–43, 2017.

[19] S. Maheshwari, R. B. Pachori, and U. R. Acharya, "Automated diagnosis of glaucoma using empirical wavelet transform and correntropy features extracted from fundus images," *IEEE J. Biomed. Health Inform.*, vol. 21, no. 3, pp. 803–813, May 2017.

[20] P. J. Foster, R. Buhrmann, H. A. Quigley, and G. J. Johnson, "The definition and classification of glaucoma in prevalence surveys," *Brit. J. Ophthalmol.*, vol. 86, no. 2, pp. 238–242, 2002.

[21] H. Springelkamp *et al.*, "Incidence of glaucomatous visual field loss after two decades of follow-up: The rotterdam study," *Eur. J. Epidemiol.*, vol. 32, no. 8, pp. 691–699, Aug. 2017.

[22] H. Springelkamp *et al.*, "Meta-analysis of genome-wide association studies identifies novel loci that influence cupping and the glaucomatous process," *Nature Commun.*, vol. 5, Sep. 2014, Art. no. 4883.

[23] P. Schneider, M. Biehl, and B. Hammer, "Adaptive relevance matrices in learning vector quantization," *Neural Comput.*, vol. 21, no. 12, pp. 3532–3561, Dec. 2009.

[24] M. C. V. S. Mary, E. B. Rajsingh, and G. R. Naik, "Retinal fundus image analysis for diagnosis of glaucoma: A comprehensive survey," *IEEE Access*, vol. 4, pp. 4327–4354, 2016.

[25] C. Sinthanayothin, J. F. Boyce, H. L. Cook, and T. H. Williamson, "Automated localisation of the optic disc, fovea, and retinal blood vessels from digital colour fundus images," *Brit. J. Ophthalmol.*, vol. 83, no. 8, pp. 902–910, 1999.

[26] T. Walter and J.-C. Klein, "Segmentation of color fundus images of the human retina: Detection of the optic disc and the vascular tree using morphological techniques," in *Proc. 2nd Int. Symp. Med. Data Anal. (ISMDA)*. New York, NY, USA: Springer-Verlag, 2001, pp. 282–287.

[27] H. Li and O. Chutatape, "Automatic location of optic disk in retinal images," in *Proc. Int. Conf. Image Process.*, vol. 2, Oct. 2001, pp. 837–840.

[28] R. Chrástek, M. Wolf, K. Donath, G. Michelson, and H. Niemann, "Optic disc segmentation in retinal images," in *Bildverarbeitung für die Medizin*. Berlin, Germany: Springer, 2002, pp. 263–266.

[29] A. Hoover and M. Goldbaum, "Locating the optic nerve in a retinal image using the fuzzy convergence of the blood vessels," *IEEE Trans. Med. Imag.*, vol. 22, no. 8, pp. 951–958, Aug. 2003.

[30] M. Foracchia, E. Grisan, and A. Ruggeri, "Detection of optic disc in retinal images by means of a geometrical model of vessel structure," *IEEE Trans. Med. Imag.*, vol. 23, no. 10, pp. 1189–1195, Oct. 2004.

[31] A. M. Mendonça, A. Sousa, L. Mendonça, and A. Campilho, "Automatic localization of the optic disc by combining vascular and intensity information," *Comp. Med. Imag. Graph.*, vol. 37, nos. 5–6, pp. 409–417, 2013.

[32] S. Roychowdhury, D. D. Koozekanani, S. N. Kuchinka, and K. K. Parhi, "Optic disc boundary and vessel origin segmentation of fundus images," *IEEE J. Biomed. Health Inform.*, vol. 20, no. 6, pp. 1562–1574, Nov. 2016.

[33] A. Salazar-Gonzalez, D. Kaba, Y. Li, and X. Liu, "Segmentation of the blood vessels and optic disk in retinal images," *IEEE J. Biomed. Health Inform.*, vol. 18, no. 6, pp. 1874–1886, Nov. 2014.

[34] M. Lalonde, M. Beaulieu, and L. Gagnon, "Fast and robust optic disc detection using pyramidal decomposition and Hausdorff-based template matching," *IEEE Trans. Med. Imag.*, vol. 20, no. 11, pp. 1193–1200, Nov. 2001.

[35] A. Osareh, M. Mirmehdi, B. Thomas, and R. Markham, "Comparison of colour spaces for optic disc localisation in retinal images," in *Proc. 16th Int. Conf. Pattern Recognit.*, vol. 16, Aug. 2002, pp. 743–746.

[36] M. N. Zahoor and M. M. Fraz, "Fast optic disc segmentation in retina using polar transform," *IEEE Access*, vol. 5, pp. 12293–12300, 2017.

[37] J. Liu *et al.*, "Optic cup and disk extraction from retinal fundus images for determination of cup-to-disc ratio," in *Proc. 3rd IEEE Conf. Ind. Electron. Appl.*, Jun. 2008, pp. 1828–1832.

[38] F. Yin *et al.*, "Automated segmentation of optic disc and optic cup in fundus images for glaucoma diagnosis," in *Proc. 25th IEEE Int. Symp. Comput.-Based Med. Syst. (CBMS)*, Jun. 2012, pp. 1–6.

[39] D. W. K. Wong *et al.*, "An ensembling approach for optic cup detection based on spatial heuristic analysis in retinal fundus images," in *Proc. Annu. Int. Conf. IEEE Eng. Med. Biol. Soc.*, Aug. 2012, pp. 1426–1429.

[40] D. W. K. Wong *et al.*, "Detecting the optic cup excavation in retinal fundus images by automatic detection of vessel kinking," in *Proc. 21st Int. Conf. Pattern Recognit.*, Nov. 2012, pp. 73–76.

[41] P. S. Mittapalli and G. B. Kande, "Segmentation of optic disk and optic cup from digital fundus images for the assessment of glaucoma," *Biomed. Signal Process. Control*, vol. 24, pp. 34–46, Feb. 2016.

[42] R. Bock, J. Meier, L. Nyül, J. Hornegger, and G. Michelson, "Glaucoma risk index: Automated glaucoma detection from color fundus images," *Med. Image Anal.*, vol. 14, no. 3, pp. 471–481, 2010.

[43] D. S. W. Ting and *et al.*, "Development and validation of a deep learning system for diabetic retinopathy and related eye diseases using retinal images from multiethnic populations with diabetes," *JAMA*, vol. 318, no. 22, pp. 2211–2223, 2017.

[44] A. A.-H. A.-R. Youssif, A. Ghalwash, A. A. Sabry, and A.-R. Ghoneim, "Optic disc detection from normalized digital fundus images by means of a vessels' direction matched filter," *IEEE Trans. Med. Imag.*, vol. 27, no. 1, pp. 11–18, Jan. 2008.

[45] A. Sevastopolsky, "Optic disc and cup segmentation methods for glaucoma detection with modification of U-Net convolutional neural network," *Pattern Recognit. Image Anal.*, vol. 27, no. 3, pp. 618–624, 2017.
[46] H. Fu, J. Cheng, Y. Xu, D. W. K. Wong, J. Liu, and X. Cao, "Joint optic disc and cup segmentation based on multi-label deep network and polar transformation," *IEEE Trans. Med. Imag.*, vol. 37, no. 7, pp. 1597–1605, Jul. 2018.
[47] M. D. Abràmoff *et al.*, "Automated segmentation of the optic disc from stereo color photographs using physiologically plausible features," *Invest. Ophthalmol. Vis. Sci.*, vol. 48, pp. 1665–1673, Apr. 2007.
[48] J. Xu *et al.*, "Automated assessment of the optic nerve head on stereo disc photographs," *Invest. Ophthalmol. Vis. Sci.*, vol. 49, no. 6, pp. 2512–2517, 2008.
[49] T. Khalil, M. U. Akram, H. Raja, A. Jameel, and I. Basit, "Detection of glaucoma using cup to disc ratio from spectral domain optical coherence tomography images," *IEEE Access*, vol. 6, pp. 4560–4576, 2018.
[50] G. Azzopardi and N. Azzopardi, "Trainable COSFIRE filters for keypoint detection and pattern recognition," *IEEE Trans. Pattern Anal. Mach. Intell.*, vol. 35, no. 2, pp. 490–503, Feb. 2013.
[51] A. Neocleous, G. Azzopardi, C. Schizas, and N. Petkov, "Filter-based approach for ornamentation detection and recognition in singing folk music," in *Computer Analysis of Images and Patterns* (Lecture Notes in Computer Science), vol. 9256. Springer, 2015, pp. 558–569.
[52] G. Azzopardi, N. Strisciuglio, M. Vento, and N. Petkov, "Trainable COSFIRE filters for vessel delineation with application to retinal images," *Med. Image Anal.*, vol. 19, no. 1, pp. 46–57, Jan. 2015.
[53] J. Guo, C. Shi, G. Azzopardi, and N. Petkov, "Recognition of architectural and electrical symbols by COSFIRE filters with inhibition," in *Computer Analysis of Images and Patterns* (Lecture Notes in Computer Science), vol. 9257. Springer, 2015, pp. 348–358.
[54] C. Shi, J. Guo, G. Azzopardi, J. M. Meijer, M. F. Jonkman, and N. Petkov, "Automatic differentiation of u- and n-serrated patterns in direct immunofluorescence images," in *Computer Analysis of Images and Patterns* (Lecture Notes in Computer Science), vol. 9256. Springer, 2015, pp. 513–521.
[55] N. Strisciuglio, G. Azzopardi, M. Vento, and N. Petkov, "Supervised vessel delineation in retinal fundus images with the automatic selection of B-COSFIRE filters," *Mach. Vis. Appl.*, vol. 27, no. 8, pp. 1137–1149, 2016.
[56] J. Guo, C. Shi, G. Azzopardi, and N. Petkov, "Inhibition-augmented trainable COSFIRE filters for keypoint detection and object recognition," *Mach. Vis. Appl.*, vol. 27, no. 8, pp. 1197–1211, 2016.
[57] L. Fernandez Robles, G. Azzopardi, E. Alegre, and N. Petkov, "Machine-vision-based identification of broken inserts in edge profile milling heads," *Robot. Comput.-Integr. Manuf.*, vol. 44, pp. 276–283, Apr. 2017.
[58] J. Guo, C. Shi, N. M. Jansonius, and N. Petkov, "Automatic optic disk localization and diameter estimation in retinal fundus images," in *Proc. 8th GI Conf. Auto. Syst.*, vol. 842, 2015, pp. 70–79.
[59] G. Papari, N. Petkov, and P. Campisi, "Artistic edge and corner enhancing smoothing," *IEEE Trans. Image Process.*, vol. 16, no. 10, pp. 2449–2462, Oct. 2007.
[60] T. Kohonen, "Learning vector quantization for pattern recognition," Helsinki Univ. Technol., Espoo, Finland, Tech. Rep. TKKF-A601, 1986.
[61] M. Biehl. (2016). *A No-Nonsense GMLVQ Toolbox*. [Online]. Available: http://matlabserver.cs.rug.nl/gmlvqweb/web/
[62] J. Sivaswamy, S. Krishnadas, G. D. Joshi, M. Jain, and A. U. S. Tabish, "Drishti-GS: Retinal image dataset for optic nerve head (ONH) segmentation," in *Proc. IEEE 11th Int. Symp. Biomed. Imag. (ISBI)*, Apr. 2014, pp. 53–56.
[63] E. J. Carmona, M. Rincón, J. García-Feijoó, and J. M. Martínez-de-la Casa, "Identification of the optic nerve head with genetic algorithms," *Artif. Intell. Med.*, vol. 43, no. 3, pp. 243–259, 2008.
[64] J. Lowell *et al.*, "Optic nerve head segmentation," *IEEE Trans. Med. Imag.*, vol. 23, no. 2, pp. 256–264, Feb. 2004.
[65] T. Köhler, A. Budai, M. F. Kraus, J. Odstrčilik, G. Michelson, and J. Hornegger, "Automatic no-reference quality assessment for retinal fundus images using vessel segmentation," in *Proc. IEEE Int. Symp. Comput.-Based Med. Syst. (CBMS)*, Jun. 2013, pp. 95–100.
[66] C. Owen *et al.*, "Measuring retinal vessel tortuosity in 10-year-old children: Validation of the computer-assisted image analysis of the retina (CAIAR) program," *Invest. Ophthalmol. Vis. Sci.*, vol. 50, no. 5, pp. 2004–2010, 2009.
[67] T. Kauppi *et al.*, "DIARETDB1 diabetic retinopathy database and evaluation protocol," in *Proc. Med. Image Understand. Anal.*, Aberystwyth, U.K., 2007, pp. 61–65.
[68] E. Decenciére *et al.*, "Feedback on a publicly distributed image database: The Messidor database," *Image Anal. Stereol.*, vol. 33, no. 3, pp. 231–234, Aug. 2014.
[69] J. D'Errico, "Inpaint_nans—File exchange MATLAB Central," Tech. Rep., Feb. 2004. [Online]. Available: https://www.mathworks.com/matlabcentral/fileexchange/4551-inpaint_nans
[70] W. Ramdas, R. Wolfs, A. Hofman, P. de Jong, H. Vingerling, and N. Jansonius, "Heidelberg retina tomograph (HRT3) in population-based epidemiology: Normative values and criteria for glaucomatous optic neuropathy," *Ophthalmic Epidemiol.*, vol. 18, no. 5, pp. 198–210, 2011.
[71] M. U. Akram, A. Tariq, S. Khalid, M. Y. Javed, S. Abbas, and U. U. Yasin, "Glaucoma detection using novel optic disc localization, hybrid feature set and classification techniques," *Australas. Phys. Eng. Sci. Med.*, vol. 38, no. 4, pp. 643–655, 2015.
[72] J. Ayub *et al.*, "Glaucoma detection through optic disc and cup segmentation using K-mean clustering," in *Proc. Int. Conf. Comput., Electron. Elect. Eng. (ICE Cube)*, Apr. 2016, pp. 143–147.
[73] A. Septiarini, A. Harjoko, R. Pulungan, and R. Ekantini, "Optic disc and cup segmentation by automatic thresholding with morphological operation for glaucoma evaluation," *Signal, Image Video Process.*, vol. 11, no. 5, pp. 945–952, 2017.
[74] M. M. de Vries, R. Stoutenbeek, R. P. H. M. Müskens, and N. M. Jansonius, "Glaucoma screening during regular optician visits: The feasibility and specificity of screening in real life," *Acta Ophthalmol.*, vol. 90, no. 2, pp. 115–121, 2012.
[75] H. Vaahtoranta-Lehtonen *et al.*, "Cost effectiveness and cost utility of an organized screening programme for glaucoma," *Acta Ophthalmol.*, vol. 85, no. 5, pp. 508–518, 2007.

JIAPAN GUO received the Ph.D. degree in visual pattern recognition and its applications in ophthalmology from the University of Groningen, in 2017. Her current research interests include brain-inspired computer vision and its medical applications, including computational visual models of feature and object recognition, image segmentation, and their applications in ophthalmology and radiology.

GEORGE AZZOPARDI received the B.Sc. degree (Hons.) in computer science from Goldsmiths, the M.Sc. degree in computer science from the Queen Mary University of London, and the Ph.D. degree *(cum laude)* in computer science from the University of Groningen, The Netherlands, in 2013. He is currently an Assistant Professor of computer science with the University of Groningen. He has (co)-authored more than 50 peer-reviewed publications. His research interests include pattern recognition, machine learning, signal processing, medical image analysis, and information systems. He is an Associate Editor of a Q1 journal.

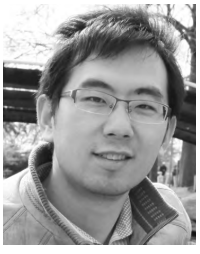

CHENYU SHI received the B.Sc. degree in electronic information engineering and the master's degree in electrification and automation from China Agricultural University (CAU), in 2009 and 2011, respectively. He is currently pursuing the Ph.D. degree with the Johann Bernoulli Institute for Mathematics and Computer Science, University of Groningen, The Netherlands. He was honored as a Technique Specialist Student with CAU. In 2010, he joined the China–Germany Public Private Partnership Project with Bonn University. His current research interests include the field of brain-inspired machine vision, which includes computational models of the visual system with applications to contour detection and feature and shape recognition.

NOMDO M. JANSONIUS received the Ph.D. degree in biophysics from the University of Groningen/Cambridge. He studied physics and medicine with the University of Groningen. He held a Postdoctoral position in physiological optics and a residency position in ophthalmology. He was a Fellow in glaucoma and neuro-ophthalmology. Since 1999, he has been an Ophthalmologist/Glaucoma Specialist with UMCG. He has (co)-authored over 100 peer-reviewed scientific papers. His current research interests include clinical studies, population-based epidemiology, psychophysics, and optical coherence tomography, all directed towards glaucoma. He is an Editorial Board Member/Associate Editor of two Q1 journals.

NICOLAI PETKOV received the Dr. sc. techn. degree in computer engineering (information-stechnik) from the Dresden University of Technology, Dresden, Germany. Since 1991, he has been a Professor of computer science and the Head of the Intelligent Systems Group, University of Groningen. He has authored two monographs, and has authored or co-authored over 150 scientific papers. He holds four patents. His current research interests include pattern recognition, machine learning, data analytics, and brain-inspired computing, with applications in healthcare, finance, surveillance, manufacturing, robotics, and animal breeding. He is a member of the editorial boards of several journals.